

Chapter 10

Phantoms for Magnetic Resonance Imaging

Reed Selwyn

10.1 Introduction

Magnetic resonance imaging (MRI) provides exceptional soft tissue contrast and is capable of generating quantitative maps to demonstrate blood flow, water diffusion, temperature distribution, and tissue relaxation properties. MRI also has widely known drawbacks such as high cost and long acquisition times. To help mitigate these factors, several fast and ultra-fast MRI protocols such as fast spin-echo (FSE) and echo-planar imaging (EPI) have been developed to reduce acquisition time while attempting to maintain image quality as measured by spatial resolution, signal-to-noise ratio (SNR), and contrast-to-noise ratio (CNR). Fast imaging protocols tend to increase image distortion and ghosting, yet they also help minimize motion and flow artifacts. Attentive and routine quality assurance tests and calibrations using MRI-specific phantoms can reduce these artifacts.

In addition to fast imaging protocols, several quantitative MRI protocols such as relaxometry, magnetization transfer, spectroscopy, diffusion, perfusion, and blood oxygen level-dependent (BOLD) imaging are used in clinics and academic centers throughout the world. Quantitative techniques strive to produce parametric maps that are then overlaid on anatomical images such as T1 or T2-weighted images. The precision and accuracy of quantitative MRI depend on factors such as magnetic field stability and uniformity, gradient field instabilities, eddy currents, RF pulse profiles, and environmental conditions. Sequence-specific phantoms are

The views expressed are those of the author and do not reflect the official policy or position of the Uniformed Services University of the Health Sciences, the Department of Defense, or the United States Government.

R. Selwyn (✉)

Department of Radiology, Uniformed Services University, Bethesda, Maryland 20814, USA
e-mail: reed.selwyn@usuhs.edu

R. Selwyn

Department of Medical Physics, University of Wisconsin, Madison, Wisconsin 53705, USA

required to calibrate, normalize, and successfully interpret across multiple MRI platforms and field strengths. However, there are only a few standard MR phantoms that are routinely used for quality assurance testing or for normalizing scanner response for supporting multicenter clinical trials. It should be noted that researchers, academic centers, and vendors have constructed unique phantoms for a singular or limited purpose.

10.2 General MRI Phantom Construction

In general, MRI phantoms are fluid-filled objects that mimic body shapes and dimensions such as the head or abdomen—most are cylindrical or spherical in shape. Phantoms can be constructed with structures to evaluate image contrast, SNR, image uniformity, spatial resolution, slice thickness, and geometric accuracy. It is important to select materials that are free from susceptibility effects or signal disruption. For example, in the brain, the magnetic susceptibility in soft tissue is -9.05×10^{-6} and in air is 0.4×10^{-6} , and these differences result in a magnetic field inhomogeneity, which is especially problematic in the orbitofrontal cortex [1]. Materials such as Perspex, acrylic, nylon, or polystyrene produce minimal susceptibility effects at water/phantom junctions and are commonly utilized. For example, acrylic introduces a 0.003 parts per million (ppm) phase shift, whereas Teflon results in a 0.03 ppm shift measured at 3T [2]. Both materials are considered acceptable for MR field measurements. The filling fluid can be doped with a solution such as copper sulfate to modify the relaxation times for expediency and to minimize temperature dependence of relaxation times. For example, the American College of Radiology (ACR) has produced a standard MRI phantom that is filled with a solution of 10 mM nickel chloride and 75 mM sodium chloride [3]. This phantom will be discussed in more detail. Vendors also provide body-specific phantoms that mimic conductivities found in the human body and electrical loading of the coil. These loading phantoms are designed to fit specific body coils and are used during acceptance testing and annual physics testing to evaluate image uniformity, ghosting, and SNR. Figure 10.1 provides a photograph of typical loading phantoms.

Fig. 10.1 A photograph showing several MRI loading phantoms provided with the General Electric Healthcare (Waukesha, WI) MRI system. Each vendor provides coil-specific loading phantoms



10.3 American College of Radiology Accreditation Phantom

MR provides exceptional soft tissue contrast with high spatial resolution (<1 mm) or ultra-high-resolution (<0.5 mm) imaging. Spatial resolution is an important parameter to evaluate, and it depends on several factors such as the field of view (FOV), the number of frequency/readout and phase encode steps, and slice thickness based on transmit bandwidth and gradient strength. Other important parameters are low-contrast detectability, geometric distortion, image uniformity, slice thickness accuracy, and signal-to-noise ratio. To evaluate these essential system parameters, a standard protocol and phantom should be used for reproducibility. For MRI accreditation, the American College of Radiology (ACR) has established a protocol comprised of a standardized T1-weighted and T2-weighted protocols and a cylindrical MRI phantom. Ihalainen et al. [4] compared 11 different MRI systems operating at field strengths of 1.0T, 1.5T, and 3.0T using the ACR accreditation head phantom. In general, the ACR protocol was simple to follow and easy to perform and allows clinicians to link quality assurance results to image quality. However, the choice of some parameters such as receiver bandwidth was not provided, and the ACR protocol does not support quality assurance testing for advanced imaging techniques such as fat saturation or spectroscopy. Commercially available ACR accreditation phantoms for head (large phantom) and knee (small phantom) are shown in Figs. 10.2 and 10.3.

The ACR generated a head phantom that is a short, hollow cylinder made from acrylic and measures 148 mm (length) and 190 mm (diameter), the same size as a typical head, and a knee phantom that is 100 mm long by 100 mm in diameter. The head phantom is filled with a solution of 10 mM NiCl and 75 mM NaCl, and the knee phantom is filled with 10 mM NiCl and 0.45 % by weight aqueous NaCl to mimic the T1 and T2 of soft tissue (ACR MRI Quality Control Manual). Several quantitative tests can be made using the structures found inside each phantom. These tests are described in detail in the *Phantom Test Guidance for the ACR MRI*

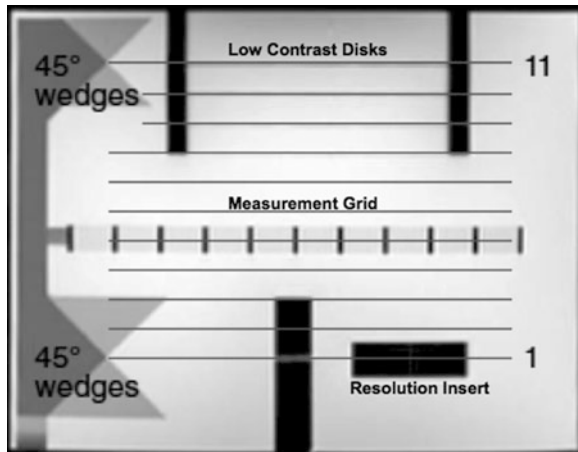
Fig. 10.2 ACR large head phantom, 148 mm (length) \times 190 mm (diameter)



Fig. 10.3 ACR small knee phantom, 100 mm (length) \times 100 mm (diameter)



Fig. 10.4 A sagittal localizer of the phantom is displayed and shows two 45° wedges, 11 axial slice locations that intersect wedges at slices 1 and 11, four low-contrast disks (slices 8–11), a resolution insert (slice 1), and measurement grid (slice 5)



Accreditation Program (www.acr.org), and this section will only present the tests in general and will focus on phantom structures.

1. **Geometric Accuracy**—Geometric accuracy describes the degree of geometric distortion and refers to either displacement or scaling errors. The scaling error is determined by measuring the length (148 mm) and diameter (190 mm) on a localizer. A sagittal localizer of the phantom is displayed in Fig. 10.4 and shows two 45° wedges, 11 axial slice locations, low-contrast disks, the resolution insert, and measurement grid at slice 5. The wedges are 2 cm in length, crossing at 1 cm, and are separated by 100 mm. Length and diameter measurements are also obtained at slice 1. Figure 10.5 shows an image of the measurement grid that consists of a 10 \times 10 array of squares that is useful for measuring the diagonal lengths (190 mm).
2. **High-Contrast Spatial Resolution**—A spatial resolution insert is located in slice 1 and consists of small holes filled with water. This insert evaluates the ability of the MRI scanner to resolve small objects with sufficient contrast. Figure 10.6a shows an image of the resolution insert with three pairs of holes that includes an upper array and a lower array, not square but skewed. The arrays share a

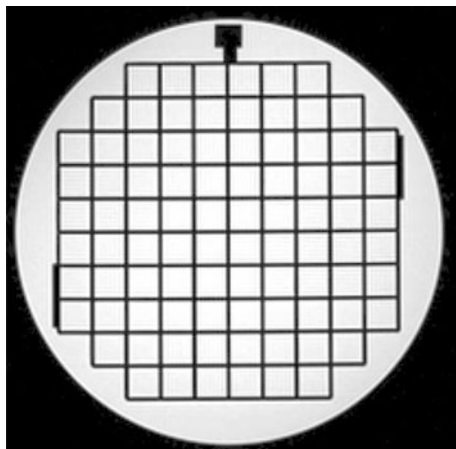


Fig. 10.5 An image of the 10×10 array comprising the measurement grid located in axial slice 5

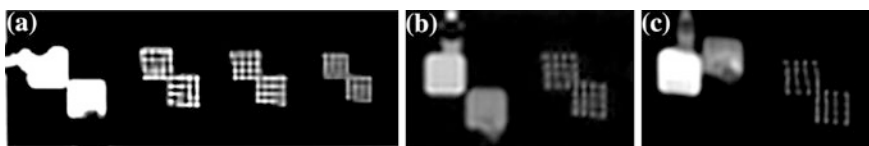


Fig. 10.6 **a** Resolution insert located in slice 1 of the ACR head phantom. **b** Chemical shift module with image acquired at $BW = 32$ kHz. The module is located to the *left* of the resolution insert. **c** Chemical shift insert with image acquired at $BW = 2$ kHz. The shift of the fat square in the A/P direction is clearly demonstrated

common hole located at the corner. The hole diameter reduces from 1.1 mm on the left pair to 0.9 mm on the right pair. The upper array has 4 rows of 4 holes that are separated by a length that is twice the hole diameter and is used to evaluate the left–right resolution. The lower array has 4 columns of 4 holes that are separated like the upper array but is used to evaluate the anterior–posterior resolution.

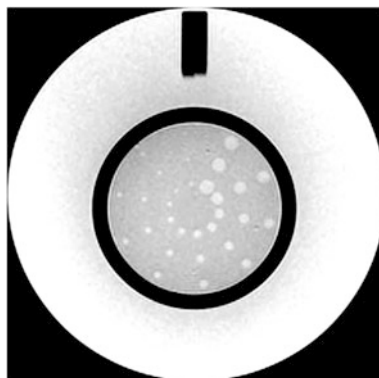
The two squares located on the left side of the resolution insert comprise a chemical shift module and provide a method to assess chemical shift and to estimate the receiver bandwidth (BW) setting. The upper square is filled with water and the lower square represents fat. Modifying the receiver BW will result in a shift in the frequency encode direction as shown in Fig. 10.6.

3. **Slice Thickness Accuracy**—There is a slice thickness insert located in slice 1 that contains 2 ramps that cross with a slope of 10:1 with respect to the plane of the slice. Therefore, the angle between the axial slice and the ramp is about 5.71° , $\tan^{-1}(1/10)$ and results in a signal that appears 10 times the thickness of the prescribed slice. The ramps are 1-mm-wide slots etched into a plastic block



Fig. 10.7 **a** Slice thickness accuracy displayed in slice 1, located directly above resolution insert. **b** Slice position accuracy is evaluated by measuring the difference in the vertical bar lengths at the *top* of the phantom

Fig. 10.8 Low-contrast detectability is evaluated by counting visible spokes in slices 8–11. Slice 11 is displayed with all spokes clearly visible



that are filled with the phantom solution since the slots are open to the phantom. Right to left tilt will be visible in the ramp signal and can help identify alignment issues (Fig. 10.7a).

4. Slice Position Accuracy—The 45° wedges shown in Fig. 10.7 are observed on slices 1 and 11 and are used to determine the slice position accuracy. Well-positioned slices will cross the wedges at the 45° intersection and will result in equally sized bars located at the top of slices 1 and 11 (Fig. 10.7b).
5. Low-Contrast Detectability—The ACR phantom has four low-contrast disks or plastic membranes located in slices 8 through 11. Each disk has a different thickness and, for the same slice thickness, a different partial volume effect. More or less volume averaging leads to a change in contrast. The contrast varies from 1.4 %, 2.5 %, 3.6 %, and 5.1 % from slice 8 to slice 11. Each disk consists of 10 spokes with 3 small holes per spoke—a total of 30 holes per slice (Fig. 10.8, slice 11). All holes in the same spoke have the same diameter but the diameter decreases, moving clockwise, from 7 to 1.5 mm.

Overall, the ACR MR phantom enables basic daily/routine QA testing by technologists and more advanced testing by medical physicists. Routine testing of the MR system provides the clinicians with important feedback and assurances of reproducibility. In addition, the ACR phantom is a useful troubleshooting tool for physicists, which also enables multiplatform, multivendor comparisons.

10.4 Alzheimer's Disease Neuroimaging Initiative Phantom

The Alzheimer's Disease Neuroimaging Initiative (ADNI) is a multicenter, multivendor MRI study focused on developing standard methods for acquiring and processing MRI data to reduce measurement uncertainty. An MRI phantom was designed to track and correct scanner performance such as post-processing gradient warping correction [5]. This imaging phantom was constructed by The Phantom Laboratory (Salem, NY) and is used to measure SNR, CNR or image contrast, and spatial distortion. The phantom, Magphan[®] Quantitative Imaging Phantom, consists of 165 spherical objects inside a 20-cm diameter, water-filled clear urethane shell. The spherical objects are 1.4-mm-thick polycarbonate shells filled with various concentrations of copper sulfate. For assessing spatial distortion, there are 158 fiducial spheres at 1.0 cm and two at 1.5-cm inner diameter (ID) filled with 0.82 g of copper sulfate pentahydrate per liter. A single 6-cm sphere filled with 0.82 g of copper sulfate pentahydrate per liter solution is used for testing SNR, and four 3-cm spheres with copper sulfate pentahydrate solutions ranging from 0.22 to 0.59 g/l are used for testing CNR or image contrast. For the 3-cm CNR spheres, the target T1 ranges from 900 to 450 ms (Magphan[®] EMR051 manual). Figure 10.9 shows the internal components of the ADNI phantom, and Fig. 10.10 provides an example of a typical distortion plot generated by the Image Owl (Salem, NY) MR Distortion Service. The photographs were provided by The Phantom Laboratory (Salem, NY).

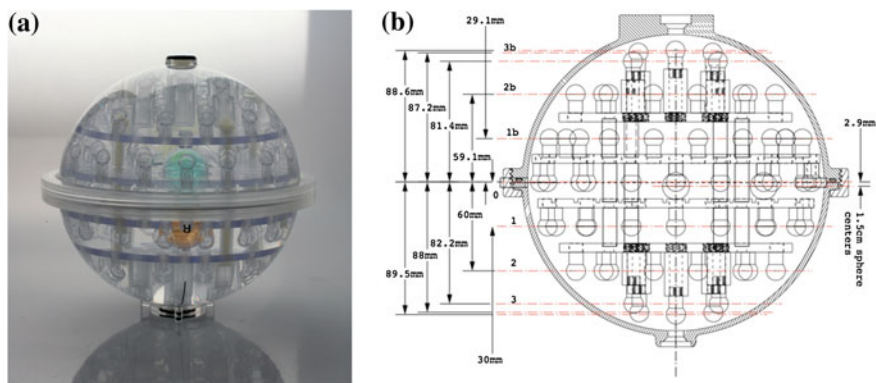


Fig. 10.9 *Left* A photograph of the Magphan[®] Quantitative Imaging Phantom. *Right* Design specifications for the imaging phantom. Photographs provided by the Phantom Laboratory (Salem, NY)



Fig. 10.10 An image distortion plot generated using Image Owl (Salem, NY) MR Distortion Service. The Magphan[®] Quantitative Imaging Phantom is scanned, and the DICOM image set is uploaded for processing. Actual and imaged sphere positions are evaluated to provide fourth-order distortion measurements

10.5 National Institute of Standards and Technology Phantom

The National Institute of Standards and Technology (NIST) has developed the first MRI phantom that is traceable to national standards [6]. The phantom shown in Fig. 10.11 is designed after the ADNI MRI phantom and ACR phantom and is nicknamed ‘Phannie’ [5]. Similar to the ADNI phantom, the NIST phantom was designed to mimic the human head and is a 20-cm water-filled spherical polycarbonate shell. There are five polyphenylene sulfide (PPS) plates connected with PPS rods. PPS was chosen due to its low water absorption and thermal expansion. The five coronal plates support 57 fiducial spheres, three arrays consisting of 14 elements each to assess T1/T2/proton density, and a resolution insert and slice profile wedges similar to the ACR phantom. The fiducial spheres are 1 cm in diameter and are located on a 4-cm three-dimensional grid. The fiducials are distributed on plates, located anterior to posterior, in groups of 5, 13, 26, 13, and 5. The T1/T2/proton density arrays are designed to be NIST traceable. The T1 array (green) is doped with various concentrations of NiCl₂ to provide a wide range of T1 values for a given field strength and temperature ($B = 1.5T$, $temp = 20\text{ }^{\circ}C$, $T1 = 22\text{--}2,000\text{ ms}$). Russek et al. [6] have evaluated the influence of inversion

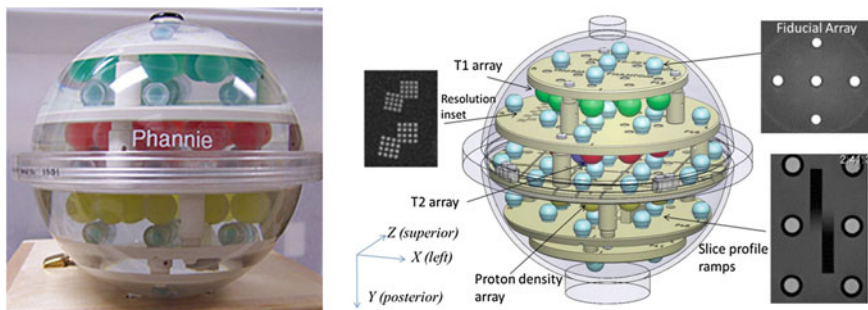


Fig. 10.11 *Left* Photograph of NIST Phannie phantom. *Right* A picture depicting the internal structure of the phantom, resolution insert, fiducial array, slice profile ramps, and location of relaxometry arrays (reproduced with permission) [6]

time, repetition time, and flip angle on measured T1 values. The T2 array (red) is doped with various concentrations of MnCl_2 to provide a wide range of T2 values for a given magnetic field strength and temperature ($B = 1.5\text{T}$, $\text{temp} = 20^\circ\text{C}$, $T_2 = 8\text{--}725\text{ ms}$). The proton density array (yellow) consists of various concentrations of deuterium and water. Eye decals are placed on the phantom shell to aid in phantom alignment in the scanner.

10.6 Magnetic Field Homogeneity Phantom

Magnetic field homogeneity throughout the field of view (FOV) is essential for high-quality, quantitative imaging. Suboptimal field homogeneity can result in poor fat and water saturation, geometric distortion, and signal loss. These effects are even more prevalent in ultra-fast imaging protocols, which are experiencing a surge in clinical applications. Initially, upon installation, the MRI is passively shimmed to eliminate field inhomogeneity introduced during shipment or from the local environment such as large iron structures near the MRI. Field homogeneity is generally described in terms of the variation in the Larmor frequency or magnetic field strength throughout the desired FOV and is expressed in ppm of the field-specific Larmor frequency or field strength. The shimming process typically results in field homogeneity of less than 0.5 ppm over a 30-cm diameter of spherical volume (DSV). Moreover, MRI vendors provide an active shim coil technique for adjusting the field homogeneity prior to each scan. Overall, field homogeneity phantoms should not perturb the field and should evaluate a clinically acceptable FOV.

Three methods for testing field homogeneity are currently supported. The ACR Magnetic Resonance Imaging Quality Control Manual, Medical Physicist's section, describes two methods: spectral peak and phase difference map. Both techniques require that a uniform, spherical phantom be placed at the isocenter of the magnet.

Fig. 10.12 A photograph of the magnetic field homogeneity phantom issued by General Electric Healthcare (Waukesha, WI) during installation of the MRI system



The manufacturer specifies the homogeneity over a DSV, and the phantom should at least cover the same DSV. The DSV may be specified up to 50 cm DSV, which can be problematic for phantom construction. This sizable, uniform phantom is typically provided by the vendor and is stored in multiple parts. Figure 10.12 shows a three-part uniformity phantom provided by General Electric (GE) that weighs over 120 lbs when fully assembled. Commercial vendors such as the Phantom Laboratory offer spherical phantoms to cover different DSVs. However, these phantoms do not include a filling solution. The homogeneity phantom is typically stored in the MRI room in order to reach thermal equilibrium. It should be noted that the two techniques referenced in the ACR manual are not always available on clinical MRI systems and vendor-specific techniques are generally used.

A third method described by Chen et al. [2] uses a bandwidth-difference technique to assess field homogeneity that is widely available. A two-piece spherical phantom was assembled using acrylic domes (25.4-cm outer diameter) and filled with distilled water doped with 0.01 mM copper sulfate to modify T1 and T2. An antibacterial agent, NaN_3 , was also added. Three acrylic plates, consisting of 108 holes (1.5 mm) drilled in each plate, were installed in the phantom. Each plate has six rows of six holes that cross at a 45° angle at the center, and the positional shift between holes is determined in two different bandwidth images. Chen et al. [2] demonstrated the difficulty in obtaining data from the spectral peak and phase shift methods.

10.7 Proton Relaxation Phantoms

MRI is widely appreciated for high-resolution, soft tissue imaging, but MRI is also quantitative and can measure several tissue-specific characteristics such as proton density and relaxation time. It should be noted that this information is not easily

converted to electron density for use with radiation treatment planning or attenuation correction for positron emission tomography imaging. Tissue-specific longitudinal relaxation time (T1) and transverse relaxation time (T2) depend on molecular motion and the local microenvironment. Therefore, tissue relaxation times that differ from normal or baseline levels may indicate inflammation, edema, microhemorrhage, or biological dysfunction. Relaxation times depend on field strength, temperature, and MRI sequence parameters. A typical sequence for measuring T1 is a 2D gradient recalled echo or spin-echo inversion recovery (GRE-IR or SE-IR) with 4 inversion times (TI) of 50, 400, 1,100, and 2,500 ms; repetition time (TR) of 2,550 ms; and echo time (TE) of 7–14 ms [7]. Measurement of T2 depends on TR settings, and Cheung et al. [8] recommends a fast radio-frequency enforced steady state (FRESS) spin echo for mapping T2 without TR effects. An optimized gold standard sequence for T2 mapping presented by Pell et al. [9] is a single spin echo, six echoes with TE between 30 and 230 ms, TR of 10 s, with a refocusing slice selection width equal to three times the excitation slice selection width. Table 10.1 shows typical T1 and T2 values for common tissues imaged at 1.5 and 3.0T measured in vitro immediately after excision [10]. It should be noted that these values are different from values published by others such as Akber et al. [11]. The reader is referred to work by Akber [11], Stanisz et al. [10], and Kato et al. [12] for recent reviews of tissue relaxation times. Overall, significant differences in measured T1 or T2 values can be expected due to differences in pulse sequence utilized.

For accurate and precise measurements of human T1 and T2 values, standardized pulse sequences are essential. Phantoms for quantifying T1 and T2 values should have relaxation times and dielectric properties that are representative of human tissues and are homogeneously distributed throughout the phantom. Phantoms have been constructed using aqueous solutions doped with paramagnetic ions such as $GdCl_3$, $MnCl_2$, $CuSO_4$, or $NiCl_2$. These phantoms provide a homogeneous solution in a rigid container but generally suffer from flow or motion artifacts. The ACR head phantom, for example, is filled with a solution of 10 mM NiCl and 75 mM NaCl and mimics general tissue relaxation times. Gelatin phantoms are also doped with paramagnetic ions but do not suffer from flow artifacts and are typically based on polyacrylamide, polyvinyl alcohol, gelatin, agarose, or agar. Recently, carrageenan was used as a gelling agent to stabilize the

Table 10.1 Typical T1 and T2 values for various tissues measured at 1.5 and 3T

Tissue	T1 values (ms)		T2 values (ms)	
	3T	1.5T	3T	1.5T
Blood	1,932 ± 85	1,441 ± 120	275 ± 50	290 ± 30
White matter	1,084 ± 45	884 ± 50	69 ± 3	72 ± 4
Gray matter	1,820 ± 114	1,124 ± 50	99 ± 7	95 ± 8
Muscle	1,412 ± 13	1,008 ± 20	50 ± 4	44 ± 6
Liver	812 ± 64	576 ± 30	42 ± 3	46 ± 6

phantom without influencing T1 or T2 values [12]. The proposed phantom also contains NaCl to modify conductivity, GdCl_3 to modify T1, agarose to modify T2, NaN_3 as an antiseptic, and distilled water. The proposed NIST phantom will also provide a traceable measurement of T1 and T2 values as discussed in earlier.

10.8 Diffusion Phantoms

Diffusion-weighted MRI provides a quantitative method to measure tissue-specific diffusion characteristics such as apparent diffusion coefficient (ADC), mean diffusivity (MD), and fractional anisotropy (FA) that can help clinicians and scientists better understand underlying brain architecture and microstructure. Diffusion tensor imaging (DTI) was introduced in the mid-1990s and provides a mathematical framework for detecting directional diffusion, both isotropic and anisotropic diffusion, for visualizing motion along tracts [13]. Diffusion techniques have been used extensively for imaging neurological dysfunction and disease such as inflammation, multiple sclerosis, traumatic axonal injury, cellular infiltration/activation, and connectivity studies [14–17].

Like other tissue-specific measurements, obtaining reliable and reproducible data is challenging and depends on several acquisition parameters such as field strength, field homogeneity, eddy current compensation, SNR, b-values, TR, TE, gradient-encoding scheme, and pulse sequence. Zhu et al. [18] conducted a multicenter study comparing DTI results and variability using a diffusion phantom and a single travelling human volunteer. A novel isotropic diffusion phantom was developed based on work by Tofts et al. [19] using three cyclic alkanes—cyclohexane, cycloheptane, and cyclooctane—contained in cylindrical polycarbonate containers to mimic white and gray matter [19]. Phantom and human data show significant inter-site differences in accuracy and precision of FA and MD values due to eddy current, gradient nonlinearity, and magnetic field inhomogeneity effects. It should also be noted that this study used the same vendor, MRI system, hardware, and software at each site. Currently, there is no gold standard technique to accurately compare measured diffusion parameters across platforms. Wang et al. [20] proposes to use the ACR head phantom with a standard spin-echo DTI, a single shot EPI readout, and a standard 30 direction gradient-encoding scheme for conducting quality assurance testing for diffusion imaging [20]. The ACR phantom is widely available, has internal structures to help minimize fluid motion, and is already used for routine QC. However, the ACR phantom does not have structured anisotropy and does not match diffusivities typically observed in human neuroimaging. These limitations could be overcome by developing a head phantom consisting of internal structures with varying diffusivities and anisotropy. In order to calibrate diffusion studies, as previously mentioned, Tofts et al. [19] proposed using alkanes for developing a phantom to mimic human tissue. However, Pierpaoli et al. [21] proposes a less toxic, less flammable solution of polyvinylpyrrolidone (PVP) as a potential isotropic phantom to assess diffusion MRI. The measured average diffusivity was independent

of diffusion time, a linear function of PVP concentration up to 50 %, and had a 2 % coefficient of variation for repeated measurements over a 15-month period. Overall, PVP has desirable properties for producing calibration phantoms to assess diffusion protocols across various platforms.

Mimicking biological anisotropic diffusion is not a simple achievement since physiological diffusion depends on cell infiltration, tract density and direction, fiber diameter, and background homogeneity. Several studies have developed and tested anisotropic diffusion phantoms, which have generally depended on embedding fibers in a homogeneous background [22–27]. These fibers vary in thickness, group density, direction, and diffusion characteristics. Phantoms were developed out of Micro-Dyneema[®] filled with saline doped with Gd, polyamide fibers wrapped around acrylic glass and glass capillaries filled with water [22, 24, 27]. Lorenz et al. [23] used a standard DW EPI sequence with 61 diffusion encoding directions and b-factors of 0 and 1,000 s/mm² to compare four different fibers with various thicknesses and fiber packing density: hemp (H), rayon (R), linen (L), and Dyneema[®] (Dy). Dy fibers provided higher FA (0.68), improved homogeneity, and minimal susceptibility artifacts. Ebrahimi et al. [26] presented a new phantom that utilized microfabrication lithography to generate channels to match neuronal structure. The phantom made of polydimethylsiloxane (PDMS), a silicon-based polymer, consisted of eight layers comprised of 100 channels 50 μm wide by 250 μm deep. The channels are filled with water to simulate fibers. However, only a few channels were tracked fully along the phantom axis due to various undesirable effects. In similar fashion, Samuel et al. constructed a 1.5 \times 1.5 cm \times 0.3 mm PDMS phantom comprised of thirty 10- μm -thick spin-casted layers with curved and straight microchannels measuring 5 μm in width and 8.7 μm (curved) or 3.6 μm (straight) spacing [28]. The water-filled MRI phantom was imaged on a Bruker Biospec 7T MRI (Bruker, Inc., Billerica, MA) using a standard 3D diffusion-weighted SE sequence with b-value of 800 s/mm². DTI showed less anisotropic diffusion than expected and quantitative results were not provided.

Unlike white matter, gray matter is comprised of randomly aligned axons and dendrites and has multiple cell types. Even though axons demonstrate anisotropic diffusion, the random alignment of axons in gray matter result in voxel mixing and isotropic diffusion measured on a macroscopic level. A double-pulsed gradient spin-echo (d-PGSE) sequence presented by Komlosh et al. [29] and Shemesh et al. [30] has the ability to measure net displacements of spins during multiple diffusion periods, which may convey details of small structures, below the voxel resolution. Komlosh et al. [31] evaluated this d-PGSE sequence with a novel gray matter phantom that is macroscopically isotropic but microscopically anisotropic. The gray matter phantom is a collection of randomly oriented 0.5 mm long fused silica glass tubes with an ID = 20 μm and OD = 90 μm (Polymicro Technologies). The glass tubes were filled with pure water by condensation of water vapor. The d-PGSE accurately measured diffusion coefficients for free diffusion approximated by Gaussian displacements, using short diffusion times (Δ), but do not accurately measure restricted diffusion. Komlosh et al. [27] describe another novel water-filled phantom consisting of two lead glass capillary array (GCA) wafers (13 mm OD

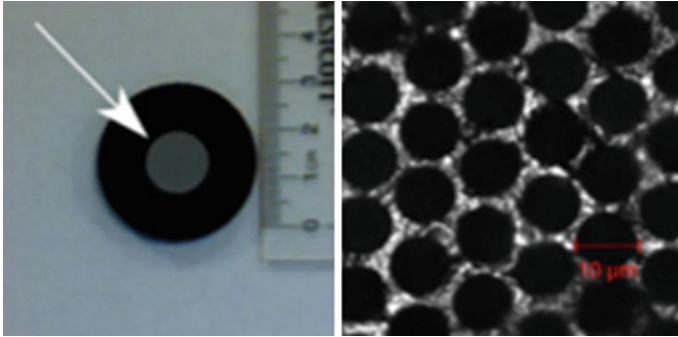


Fig. 10.13 *Left* A photograph of the 13-mm glass capillary array phantom proposed by Komlosh et al. *Right* A confocal transmission image of the microcapillaries

each) with microcapillaries of 10 μm pore diameter and 500 μm thickness. Unlike the gray matter phantom, this phantom is coherently organized and the GCA wafers are macroscopically homogeneous. Figure 10.13 shows a photograph of the 13-mm disk and confocal transmission image of the microcapillaries. Measurements of the pore diameter using the d-PGSE sequence were within 5 % of expected diameter [29, 30]. These results are partially due to the phantom having closely packed fiber arrays, 12 μm center-to-center, which provides increased pore volume and, as a result, high MR signal that is essential for diffusion MRI measurements. The GCA wafers are available in various pore sizes and diameters and can be stacked together to form a more heterogeneous diffusion phantom. The GCA phantom can be used to calibrate and validate MRI measurements of pore diameter and diameter distribution.

Overall, to improve the quality of multicenter, multivendor, or multisystem diffusion MRI studies, it is essential to develop and widely distribute a gold standard diffusion phantom that can calibrate measurements associated with free and restrained diffusion as well as small pore diameter measurements.

10.9 Temperature Considerations

The temperature of the sample directly influences the parameters measured from proton-weighted, T1-weighted, T2-weighted, diffusion and spectroscopy protocols. This temperature dependence can negatively affect quantitative measurements but can also provide useful clinical information regarding tissue temperature. Several thermal energy deposition techniques such as laser-induced thermotherapy, high-intensity focused ultrasound, and radiofrequency (RF) ablation or microwave heating can be used to noninvasively sensitize or ablate tumors [32]. The ability to accurately deliver a known temperature and to confirm delivery of desired treatment is paramount for clinical effectiveness. MRI is a useful tool

for noninvasively guiding thermal treatments by producing near real-time temperature maps or thermometry imaging [33]. Three methods for MR thermometry have been widely studied: T1 mapping, Brownian motion and diffusion, and chemical shift (CS) or proton resonance frequency (PRF) [34].

Since magnetic susceptibility is inversely proportional to temperature and the equilibrium magnetization is proportional to susceptibility, the signal obtained in a proton-weighted MR sequence decreases as the temperature increases if properly controlled for perfusion effects in vivo [34, 35]. This temperature dependence is small, approximately $0.3 \text{ \%}/^\circ\text{C}$ and, as a result, proton-weighted MR thermometry requires high SNR and long repetition times. For T1-weighted imaging, the spin–lattice interaction prolongs the relaxation time, or recovery of longitudinal magnetization, as temperature increases. Since the spin–lattice interaction varies by tissue, the temperature dependence also varies by tissue. For example, the temperature dependence in the liver is approximately $1\text{--}2 \text{ \%}/^\circ\text{C}$ and $0.97 \text{ \%}/^\circ\text{C}$ for fat [36–39]. This is an important consideration for quantitative T1 mapping for MR thermometry. Overall, the T1-weighted signal decreases as temperature increases due to the previously discussed reduction in equilibrium magnetization and increased T1 times. Kraft et al. [40] investigated the temperature dependence of T1 on phantoms comprised of gel doped with paramagnetic copper (Cu^{+2}), manganese (Mn^{+2}), and nickel (Ni^{+2}) ions. The T1 values at 100 MHz for Ni^{+2} -doped agar gels demonstrated insignificant temperature dependence, whereas Cu^{+2} - and Mn^{+2} -doped gels showed a significant temperature dependence ($10 \text{ ms}/^\circ\text{C}$) that also varied with ion concentration levels [40, 41]. This is an important factor when selecting a phantom filling solution such as NiCl. Unlike T1 measurements, T2 values determined using a T2-weighted protocol show little temperature dependence or dependence on ion concentration. This is beneficial information for phantom construction, but it is also indicates that T2 mapping is not a viable technique for MR thermometry.

Water diffusion can also serve as a thermal indicator. Molecular diffusion is based on thermal Brownian motion, and there is a direct relationship between diffusion coefficients and temperature based on the Stokes–Einstein relationship [42]. An initial study by Delannoy et al. [43] shows that the diffusion coefficient increases $2.4 \text{ \%}/^\circ\text{C}$ for a polyacrylamide gel phantom doped with 5 mM of copper sulfate using a 1.5T MRI, whereas Le Bihan et al. [44] measured $2.8 \text{ \%}/^\circ\text{C}$ at 0.5T. Results in phantom show good accuracy, subcentimeter resolution, and relatively fast acquisition times [45]. In vivo diffusion measurements clearly show an increase in contrast related signal between heated and unheated tissue as temperature increased in New Zealand rabbit brains [46]. In order to identify appropriate phantom filling solutions for diffusion imaging, Tofts et al. [19] obtained diffusion coefficients for 15 liquids, alkanes, over a temperature range of $15\text{--}30 \text{ }^\circ\text{C}$. Results indicated that n-tridecane has a diffusion coefficient similar to normal white matter with reasonable T1 and T2 values. Overall, diffusion techniques are more sensitive to temperature effects when compared to relaxometry but diffusion-related signal variations are difficult to interpret due to competing physiological factors such as tissue coagulation as temperature increases.

Due to the complexities associated with diffusion-based thermometry, researchers have evaluated the proton chemical shift or resonant frequency drift, which depends on temperature. The temperature dependence of the proton resonance frequency (PRF) is a function of the screening constant and the magnetic susceptibility constant [47, 48]. The fraction and state of hydrogen bonds in water vary as a function of temperature. As a result, there is less effective molecular screening, a drift in the local magnetic field, and a related shift in the PRF. In addition, as previously discussed, the equilibrium magnetization is proportional to the local magnetic susceptibility, which is inversely proportional to temperature. In attempt to characterize these two factors, using pure water in gel and porcine muscle and fat tissue, De [49] showed that susceptibility effects were negligible for muscle but dominate for fat tissue and that the screening constant is the same for water and muscle tissue. Similarly, Ishihara et al. [50] showed that the water proton chemical shift for pure water (-0.01 ppm/ $^{\circ}\text{C}$) is similar to the shift for different tissues measured in vitro, thereby eliminating the requirement for individual tissue calibration curves. Bertsch et al. [41] compared temperature maps generated based on chemical shift and T1 relaxation for homogeneous gel and heterogeneous muscle phantoms. The chemical shift method proved to be more accurate for homogeneous media but less accurate for fat containing media. In general, susceptibility effects can be ignored in muscle tissue but will lead to errors and reduce measurement accuracy in fat tissue. This is an important consideration for thermometry measurements and calibration using dedicated tissue-specific phantoms. Olsrud et al. [51] investigated the PRF shift using interstitial laser thermotherapy in several tissue-like phantoms such as 2 % agarose gel, pure water, porcine liver, and white of eggs. A mostly linear relationship was identified for PRF shift and temperature change in agarose gel. The reported temperature dependence for agarose gel was 0.0085 ppm/ $^{\circ}\text{C}$, which is slightly less than pure water dependence of 0.01 ppm/ $^{\circ}\text{C}$. However, successful calibration ensured that gel and water provided the same results. This phantom is applicable over a wide temperature range and can be configured in several geometries. Because PRF provides accurate temperature measurements over a wide temperature range, varies linearly with temperature, and is independent of tissue changes, PRF is a highly suitable technique for thermometry.

References

1. Yoder, D. A., et al. (2004). MRI simulator with object-specific field map calculations. *Magnetic Resonance Imaging*, 22(3), 315–328.
2. Chen, H.-H., et al. (2006). Routine testing of magnetic field homogeneity on clinical MRI systems. *Medical Physics*, 33(11), 4299–4306.
3. Jackson, E. et al. (2010). *Acceptance testing and quality assurance procedures for magnetic resonance imaging facilities*. In M. J. Bronskill et al. (Eds.), College park: American association of physicists in medicine.

4. Ihalainen, T.M. et al. (2011). MRI quality assurance using the ACR phantom in a multi-unit imaging center. *Acta oncologica*, 50(6), pp. 966–972, (Stockholm, Sweden).
5. Gunter, J. L., et al. (2009). Measurement of MRI scanner performance with the ADNI phantom. *Medical Physics*, 36(6), 2193–2205.
6. Russek, S. et al. (2012). Characterization of NIST/ISMRM MRI system phantom. *Proc. Intl. Soc. Mag. Reson. Med.*, p. 2456.
7. Barral, J. K., et al. (2010). A robust methodology for in vivo T1 mapping. *Magnetic resonance in medicine : Official Journal of the Society of Magnetic Resonance in Medicine/ Society of Magnetic Resonance in Medicine*, 64(4), 1057–1067.
8. Cheung, J. S., et al. (2012). Fast radio-frequency enforced steady state (FRESS) spin echo MRI for quantitative T2 mapping: Minimizing the apparent repetition time (TR) dependence for fast T2 measurement. *NMR in Biomedicine*, 25(2), 189–194.
9. Pell, G. S., et al. (2006). Optimized clinical T2 relaxometry with a standard CPMG sequence. *Journal of Magnetic Resonance Imaging : JMRI*, 23(2), 248–252.
10. Stanisiz, G. J., et al. (2005). T1, T2 relaxation and magnetization transfer in tissue at 3T. *Magnetic Resonance in Medicine : Official journal of the Society of Magnetic Resonance in Medicine/Society of Magnetic Resonance in Medicine*, 54(3), 507–512.
11. Akber, S. F. (2008). Water proton relaxation times of pathological tissues. *Physiological Chemistry and Physics and Medical NMR*, 40, 1–42.
12. Kato, H. et al. (2005). Composition of MRI phantom equivalent to human tissues. *Medical Physics*, 32(10), pp. 3199–3208. Available at: <http://eutils.ncbi.nlm.nih.gov/entrez/eutils/elink.fcgi?dbfrom=pubmed&id=16279073&retmode=ref&cmd=prlinks&holding=uwisclib&otool=uwisclib>.
13. Basser, P. J., Mattiello, J., & LeBihan, D. (1994). MR diffusion tensor spectroscopy and imaging. *Biophysical Journal*, 66(1), 259–267.
14. Sundgren, P. C., et al. (2004). Diffusion tensor imaging of the brain: Review of clinical applications. *Neuroradiology*, 46(5), 339–350. Springer.
15. Le Bihan, D. (2003). Looking into the functional architecture of the brain with diffusion MRI. *Nature Reviews Neuroscience*, 4(6), 469–480.
16. Beaulieu, C. (2002). The basis of anisotropic water diffusion in the nervous system—a technical review. *NMR in Biomedicine*, 15(7–8), 435–455.
17. Van Boven, R. W., et al. (2009). Advances in neuroimaging of traumatic brain injury and posttraumatic stress disorder. *The Journal of Rehabilitation Research and Development*, 46(6), 717.
18. Zhu, T., et al. (2011). Quantification of accuracy and precision of multi-center DTI measurements: a diffusion phantom and human brain study. *NeuroImage*, 56(3), 1398–1411.
19. Tofts, P. S., et al. (2000). Test liquids for quantitative MRI measurements of self-diffusion coefficient in vivo. *Magnetic Resonance in Medicine : Official journal of the Society of Magnetic Resonance in Medicine/Society of Magnetic Resonance in Medicine*, 43(3), 368–374.
20. Wang, Z. J., et al. (2011). A quality assurance protocol for diffusion tensor imaging using the head phantom from American college of radiology. *Medical Physics*, 38(7), 4415–4421.
21. Pierpaoli, C. et al. (2009). Polyvinylpyrrolidone (PVP) water solutions as isotropic phantoms for diffusion MRI studies. In *ISMRM 17th Annual Meeting and Exhibition, Honolulu, Hawai'i*. April 18–24, p. 1414.
22. Fieremans, E. et al. (2005). A flexible hardware phantom for validation of diffusion imaging sequences. In *Proc. Intl. Soc. Mag. Reson. Med.* 13, p. 1301.
23. Lorenz, R., Kreher, B.W. & Hennig, J. (2006). Anisotropic Fiber Phantom for DTI validation on a clinical scanner. *Proceedings of ISMRM 14th Scientific Meeting. Seattle, USA*.
24. Laun, F.B. et al. (2007). Investigation of a DTI-phantom with properties similar to in vivo neuronal tissue. *Proc Intl Mag Reson Med Berlin*, 15, p.1526.
25. Sadleir, R. J., et al. (2009). A controllably anisotropic conductivity or diffusion phantom constructed from isotropic layers. *Annals of Biomedical Engineering*, 37(12), 2522–2531.

26. Ebrahimi, B. et al., (2010). A microfabricated phantom for diffusion tensor imaging. *SPIE Medical*, pp.76261Q–76261Q–8.
27. Komlosh, M. E., et al. (2011). Pore diameter mapping using double pulsed-field gradient MRI and its validation using a novel glass capillary array phantom. *Journal of Magnetic Resonance*, 208(1), 128–135.
28. Samuel, R., et al. (2011). Microfluidic laminate-based phantom for diffusion tensor-magnetic resonance imaging (DT-MRI). *Journal of Micromechanics and Microengineering: Structures, Devices, and Systems*, 21(9), 950271–9502711.
29. Komlosh, M. E., et al. (2008). Observation of microscopic diffusion anisotropy in the spinal cord using double-pulsed gradient spin echo MRI. *Magnetic Resonance in Medicine : Official journal of the Society of Magnetic Resonance in Medicine/Society of Magnetic Resonance in Medicine*, 59(4), 803–809.
30. Shemesh, N., et al. (2010). From single-pulsed field gradient to double-pulsed field gradient MR: Gleaning new microstructural information and developing new forms of contrast in MRI. *NMR in Biomedicine*, 23(7), 757–780.
31. Komlosh, M. E., et al. (2007). Detection of microscopic anisotropy in gray matter and in a novel tissue phantom using double Pulsed Gradient Spin Echo MR. *Journal of magnetic resonance*, 189(1), 38–45. (San Diego, Calif.: 1997).
32. Bozzini, G., et al. (2013). Focal therapy of prostate cancer: Energies and procedures. *Urologic oncology*, 31(2), 155–167.
33. Turner, R. & Streicher, M. (2012). Measuring temperature using MRI: a powerful and versatile technique. *New York: Magma*, 25(1), pp. 1–3.
34. Rieke, V., & Butts Pauly, K. (2008). MR thermometry. *Journal of Magnetic Resonance Imaging*, 27(2), 376–390.
35. Young, I. R., et al. (1994). Further observations on the measurement of tissue T1 to monitor temperature in vivo by MRI. *Magnetic Resonance in Medicine*, 31(3), 342–345.
36. Bottomley, P. A. (1984). A review of normal tissue hydrogen NMR relaxation times and relaxation mechanisms from 1 to 100 MHz: Dependence on tissue type, NMR frequency, temperature, species, excision, and age. *Medical Physics*, 11(4), 425.
37. Bottomley, P. A. (1987). A review of 1H nuclear magnetic resonance relaxation in pathology: Are T1 and T2 diagnostic? *Medical Physics*, 14(1), 1.
38. Matsumoto, R., et al. (1994). Tissue temperature monitoring for thermal interventional therapy: Comparison of T1-weighted MR sequences. *Journal of Magnetic Resonance Imaging*, 4(1), 65–70.
39. Hynynen, K., et al. (2000). Temperature monitoring in fat with MRI. *Magnetic Resonance in Medicine : Official Journal of the Society of Magnetic Resonance in Medicine/Society of Magnetic Resonance in Medicine*, 43(6), 901–904.
40. Kraft, K. A., et al. (1987). An MRI phantom material for quantitative relaxometry. *Magnetic Resonance in Medicine*, 5(6), 555–562.
41. Bertsch, F., et al. (1998). Non-invasive temperature mapping using MRI: Comparison of two methods based on chemical shift and T1-relaxation. *Magnetic Resonance Imaging*, 16(4), 393–403.
42. Einstein, A. (1905). On the movement of small particles suspended in stationary liquids required by the molecular-kinetic theory of heat. *Annalen der Physik*, 17, 549.
43. Delannoy, J., et al. (1991). Noninvasive temperature imaging using diffusion MRI. *Magnetic Resonance in Medicine*, 19(2), 333–339.
44. Le Bihan, D., Delannoy, J., & Levin, R. L. (1989). Temperature mapping with MR imaging of molecular diffusion: application to hyperthermia. *Radiology*, 171(3), 853–857.
45. Zhang, Y., et al. (1992). On the accuracy of noninvasive thermometry using molecular diffusion magnetic resonance imaging. *International journal of hyperthermia*, 8(2), 263–274.
46. Bleier, A. R., et al. (1991). Real-time magnetic resonance imaging of laser heat deposition in tissue. *Magnetic Resonance in Medicine : Official journal of the Society of Magnetic Resonance in Medicine/Society of Magnetic Resonance in Medicine*, 21(1), 132–137.

47. Schneider, W. G., Bernstein, H. J., & Pople, J. A. (1958). Proton magnetic resonance chemical shift of free (gaseous) and associated (liquid) hydride molecules. *The Journal of Chemical Physics*, 28(4), 601.
48. Hindman, J. C. (1966). Proton resonance shift of water in the gas and liquid states. *The Journal of Chemical Physics*, 44(12), 4582–4592.
49. Poorter, J. D. (1995). Noninvasive MRI thermometry with the proton resonance frequency method: Study of susceptibility effects. *Magnetic Resonance in Medicine*, 34(3), 359–367.
50. Ishihara, Y., et al. (1995). A precise and fast temperature mapping using water proton chemical shift. *Magnetic Resonance in Medicine*, 34(6), 814–823.
51. Olsrud, J., et al. (1999). MRI thermometry in phantoms by use of the proton resonance frequency shift method: Application to interstitial laser thermotherapy. *Physics in Medicine and Biology*, 43(9), 2597–2613.
52. American College of Radiology. *Site Scanning Instructions for Use of the MR Phantom for the ACR*, Reston: The American College of Radiology. Available at: <http://www.acr.org>.